

Two-Dimensional Nonseparable Fractional Fourier Transform: Theory and Application*

Daxiang Li[†], Zhichao Zhang[‡], and Wei Yao[†]

Abstract. The one-dimensional (1D) fractional Fourier transform (FRFT) generalizes the 1D Fourier transform, offering significant advantages in time-frequency analysis of non-stationary signals. To extend the benefits of the 1D FRFT to higher-dimensional signals, 2D FRFTs, such as the 2D separable FRFT (SFRFT), gyrator transform (GT), and coupled FRFT (CFRFT), have been developed. However, existing 2D FRFTs suffer from several limitations: (1) a lack of theoretical uniformity and general applicability, (2) an inability to handle 2D non-stationary signals with nonseparable terms, and (3) failure to maintain a consistent 4D rotational relationship with the 2D Wigner distribution (WD), which is essential for ensuring geometric consistency and symmetry in time-frequency analysis. These limitations restrict the methods' performance in practical applications, such as radar, communication, sonar, and optical imaging, in which nonseparable terms frequently arise. To address these challenges, we introduce a more general definition of the 2D FRFT, termed the 2D nonseparable FRFT (NSFRFT). The 2D NSFRFT has four degrees of freedom, includes the 2D SFRFT, GT, and CFRFT as special cases, and maintains a more general 4D rotational relationship with the 2D WD. We derive its properties and present three discrete algorithms, two of which are fast algorithms with computational complexity $O(N^2 \log N)$ comparable to that of the 2D SFRFT. Numerical simulations and experiments demonstrate the superior performance of the 2D NSFRFT in applications such as image encryption, decryption, filtering, and denoising.

Key words. Fourier transform, fractional Fourier transform, two-dimensional nonseparable fractional Fourier transform, Wigner distribution

MSC codes. 26A33, 42A38, 94A08, 94A12

1. Introduction. The one-dimensional (1D) fractional Fourier transform (FRFT) [2–4, 10, 28, 31, 49, 52, 57, 62, 66], a generalization of the 1D Fourier transform (FT), offers notable advantages in processing non-stationary signals, improving signal resolution, and analyzing time-frequency characteristics. Owing to its extensive application potential, the 1D FRFT has been widely utilized in areas such as optical system analysis [13, 35–37, 46, 54], filter design [9, 18, 33, 42, 63], differential equation solving [14, 24, 25, 31], phase retrieval [15, 51, 60, 61], and pattern recognition [11, 17, 29, 48, 68]. A well-known property of the 1D FRFT is its rotational transformation relationship with the 1D Wigner distribution (WD), where the 1D

*Submitted to the editors June 29, 2025.

Funding: The work of the authors was partially supported by the Open Foundation of Hubei Key Laboratory of Applied Mathematics (Hubei University) grant HBAM202404, the Foundation of Key Laboratory of System Control and Information Processing, Ministry of Education grant Scip20240121, the Foundation of Key Laboratory of Computational Science and Application of Hainan Province grant JSKX202401, and the Foundation of Key Laboratory of Numerical Simulation of Sichuan Provincial Universities grant KLNS–2024SZFZ005.

[†]School of Mathematics and Statistics, Nanjing University of Information Science and Technology, Nanjing 210044, China (ldx200101@163.com, yaowei@nuist.edu.cn).

[‡]Corresponding author. School of Mathematics and Statistics, Nanjing University of Information Science and Technology, Nanjing 210044, China, Hubei Key Laboratory of Applied Mathematics, Hubei University, Wuhan 430062, China, and Key Laboratory of System Control and Information Processing, Ministry of Education, Shanghai Jiao Tong University, Shanghai 200240, China (zcc910731@163.com).

FRFT can be interpreted as a rotation of the 1D WD in the time-frequency plane [1, 34, 39], enabling flexible adjustments of signal time-frequency aggregation. This property makes it highly effective for tasks such as denoising, signal compression, and the separation of mixed signals.

The increasing demand for non-stationary signal processing has brought the 2D FRFT into focus [41, 44, 45, 47, 64, 65, 67]. The 2D FRFT is anticipated to extend the rotational property of the 1D FRFT, offering a robust tool for the time-frequency analysis of 2D signals. This capability is essential for handling complex 2D non-stationary signals, with applications in image processing, 2D spectral analysis, and radar imaging.

However, the definition and property analysis of the 2D FRFT are inherently more complex than those of its 1D counterpart, primarily because effectively handling nonseparable terms and rotational transformations of 2D signals is challenging. In the existing literature, the 2D separable FRFT (SFRFT) [47] extends the 1D FRFT by independently applying it along two orthogonal directions of a 2D signal. While this simplicity makes the method easy to implement in engineering applications, it limits the ability to capture 2D signals with non-separable terms. As a result, the 2D SFRFT, defined by the tensor product of two 1D FRFTs, suffers from significant challenges when processing 2D non-stationary signals with such coupling. To address this limitation, researchers have proposed more general definitions of the 2D FRFT. In 1998, Sahin *et al.* introduced the nonseparable 2D FRFT [45] to overcome the directional independence inherent in the SFRFT. Despite this innovation, the nonseparable 2D FRFT failed to maintain the 4D rotational relationship with the 2D WD. Its mathematical formulation lacked theoretical symmetry and geometric consistency, thereby restricting its effectiveness in time-frequency analysis. In 2007, Rodrigo *et al.* introduced the gyrator transform (GT) [44], which is sometimes classified as a kind of 2D nonseparable FRFT [41], capable of inducing rotations in the twisted space/spatial-frequency planes. Later, in 2017, Zayed introduced the coupled FRFT (CFRFT) [65] by leveraging a new family of Hermite functions of two complex variables. Both the GT and CFRFT exhibit a 4D rotational transformation relationship with the 2D WD, which resolved the rotational consistency issue for 2D signals and provided a novel framework for time-frequency analysis. Nonetheless, neither the GT nor the CFRFT include the 2D SFRFT as a special case. Instead, their relationship with the 2D SFRFT is intersecting rather than inclusive (see Figure 1.1), thus resulting in lacking uniformity and having limited applicability in specific scenarios.

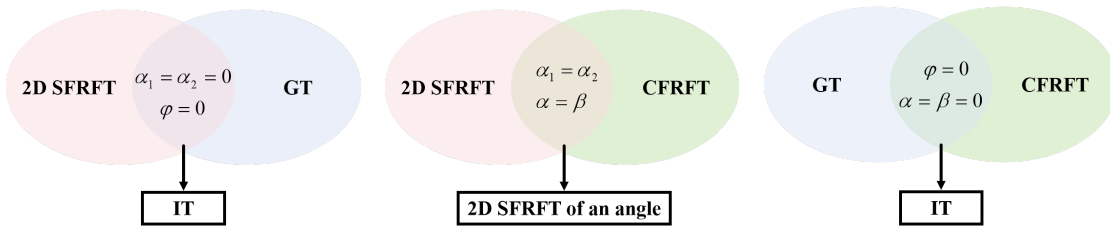


Figure 1.1. The relationship between the 2D SFRFT, GT, and CFRFT. Here, α_1, α_2 are the parameters of the 2D SFRFT, φ is the parameter of the GT, and α, β are the parameters of the CFRFT. The abbreviation "IT" denotes the 2D identity transform (IT).

Despite advancements in the theoretical and practical aspects of the 2D FRFT, a unified and universal definition remains elusive. An ideal 2D FRFT should meet the following criteria: It must possess sufficient degrees of freedom to handle 2D non-stationary signals with nonseparable terms; it should incorporate the 2D SFRFT, GT, and CFRFT as special cases to ensure theoretical comprehensiveness; and it must establish a 4D rotational relationship with the 2D WD, ensuring geometric consistency and symmetry in time-frequency analysis. Meeting these requirements would significantly advance the theoretical framework of the FRFT and provide a more flexible and efficient tool for processing 2D non-stationary signals, with expanded applications in areas such as signal processing, image analysis, and communications. The primary contributions of this study are as follows:

- We introduce the 2D nonseparable FRFT (NSFRFT), a more general definition of the 2D FRFT that incorporates four degrees of freedom and unifies the existing 2D SFRFT, GT, and CFRFT as special cases. This provides a comprehensive framework and a more general 4D rotational relationship with the 2D WD, which is crucial for geometric consistency and symmetry in time-frequency analysis.
- The 2D NSFRFT demonstrates a distinct ability to effectively process 2D chirp signals with nonseparable terms, overcoming limitations of conventional transforms such as 2D SFRFT, GT, CFRFT, and FT, which fail to handle these signals adequately.
- We develop discrete algorithms for the 2D NSFRFT, including a direct method and two fast algorithms based on matrix decomposition, with computational complexity $O(N^2 \log N)$ comparable to that of the 2D SFRFT.
- The 2D NSFRFT extends classical applications like image encryption, decryption, and optimal filtering, and enables the design of bandpass and bandstop filters for selective filtering of 2D chirp signals. Numerical experiments and comparative evaluations show that the 2D NSFRFT outperforms traditional 2D transforms, including the 2D FT, 2D SFRFT, GT, and CFRFT.

The remaining sections of this paper are organized as follows. Section 2 presents the relevant preliminary concepts. Section 3 defines the 2D NSFRFT, explores its properties, provides its geometric interpretation and highlights its unique advantage to handle 2D chirp signals with nonseparable terms. Section 4 details its discrete algorithms, including the direct method and two fast algorithms, and evaluates their performance through numerical simulations. Section 5 covers practical applications, such as image encryption, decryption, optimal filtering, and bandpass and bandstop filtering. Finally, Section 6 summarizes the findings and outlines potential directions for future research.

2. Preliminaries.

2.1. Several definitions of the FRFT.

Definition 2.1. *The 1D FRFT of a signal $f(x)$ is defined by:*

$$(2.1) \quad \mathcal{F}_\alpha[f](u) = F_\alpha(u) = \int_{\mathbb{R}} f(x) K_\alpha(u, x) dx,$$

where

$$(2.2) \quad K_\alpha(u, x) = \begin{cases} A_\alpha e^{j[\frac{\cot \alpha}{2}(x^2+u^2) - \csc \alpha ux]}, & \alpha \neq p\pi \\ \delta(u-x), & \alpha = 2p\pi \\ \delta(u+x), & \alpha = (2p \pm 1)\pi \end{cases}$$

is the kernel of the 1D FRFT with $A_\alpha = \sqrt{\frac{1-j \cot \alpha}{2\pi}}$, $\alpha = \frac{p\pi}{2}$, where p is an integer and $\delta(\cdot)$ denotes the Dirac delta function.

Note that the kernel of the 1D FRFT reduces to that of the 1D FT for $\alpha = \frac{\pi}{2}$.

Definition 2.2. The 2D SFRFT is defined by taking the tensor product of two copies of the 1D FRFTs. That is

$$(2.3) \quad \mathcal{F}_{\alpha_1, \alpha_2}[f](u, v) = F_{\alpha_1, \alpha_2}(u, v) = \int_{\mathbb{R}^2} f(x, y) K_{\alpha_1}(u, x) K_{\alpha_2}(v, y) dx dy,$$

where K_{α_i} , $i = 1, 2$ are kernels of the 1D FRFT given by (2.2).

Definition 2.3. The GT of a signal $f(x, y)$ is defined by

$$(2.4) \quad \mathcal{F}_\varphi[f](u, v) = F_\varphi(u, v) = \frac{|\csc \varphi|}{2\pi} \int_{\mathbb{R}^2} \exp \left\{ \frac{j(uv + xy)}{\tan \varphi} - \frac{j(uy + vx)}{\sin \varphi} \right\} f(x, y) dx dy.$$

Definition 2.4. The CFRFT of a signal $f(x, y)$ is defined by

$$(2.5) \quad \mathcal{F}_{\alpha, \beta}[f](u, v) = F_{\alpha, \beta}(u, v) \int_{\mathbb{R}^2} f(x, y) K_{\alpha, \beta}(x, y, u, v) dx dy,$$

where

$$(2.6) \quad K_{\alpha, \beta}(x, y, u, v) = d(\gamma) \exp \{ a(\gamma)(x^2 + y^2 + u^2 + v^2) - b(\gamma, \delta)(ux + vy) - c(\gamma, \delta)(vx - uy) \}$$

with $a(\gamma) = \frac{j \cot \gamma}{2}$, $b(\gamma, \delta) = \frac{j \cos \delta}{\sin \gamma}$, $c(\gamma, \delta) = \frac{j \sin \delta}{\sin \gamma}$, $d(\gamma) = -\frac{je^{j\gamma}}{2\pi \sin \gamma}$, and where $\gamma = \frac{\alpha + \beta}{2}$ and $\delta = \frac{\alpha - \beta}{2}$.

2.2. The Wigner distribution (WD). The WD is one of the most important and widely used time-frequency analysis tools. It is closely related to the FRFT and has numerous applications in quantum mechanics, signal analysis and optics [5–7, 27, 30, 43, 59, 69, 70].

Definition 2.5. The 1D WD of a signal $f(x)$ is defined by

$$(2.7) \quad W_f(x, u) = \int_{\mathbb{R}} f\left(x + \frac{\tau}{2}\right) f^*\left(x - \frac{\tau}{2}\right) e^{-ju\tau} d\tau,$$

where $*$ denotes the complex conjugate operator.

There is a rotational transformation relationship between the 1D FRFT and the 1D WD, that is, the 1D WD W_{F_α} of the 1D FRFT F_α of a function f equals to a 2D rotation of the 1D WD W_f of the function f , and the corresponding 2D rotation matrix \mathbf{R}_{2D} is

$$(2.8) \quad \mathbf{R}_{2D} = \begin{bmatrix} \cos \alpha & -\sin \alpha \\ \sin \alpha & \cos \alpha \end{bmatrix}.$$

Similarly, the 2D SFRFT, GT, and CFRFT all exhibit rotational transformation relationships with the 2D WD, the corresponding 4D rotation matrices \mathbf{R}_{4D}^S , \mathbf{R}_{4D}^G and \mathbf{R}_{4D}^C are

$$(2.9) \quad \mathbf{R}_{4D}^S = \begin{bmatrix} \cos \alpha_1 & 0 & -\sin \alpha_1 & 0 \\ 0 & \cos \alpha_2 & 0 & -\sin \alpha_2 \\ \sin \alpha_1 & 0 & \cos \alpha_1 & 0 \\ 0 & \sin \alpha_2 & 0 & \cos \alpha_2 \end{bmatrix},$$

$$(2.10) \quad \mathbf{R}_{4D}^G = \begin{bmatrix} \cos \varphi & 0 & 0 & -\sin \varphi \\ 0 & \cos \varphi & -\sin \varphi & 0 \\ 0 & \sin \varphi & \cos \varphi & 0 \\ \sin \varphi & 0 & 0 & \cos \varphi \end{bmatrix}$$

and

$$(2.11) \quad \mathbf{R}_{4D}^C = \begin{bmatrix} \cos \gamma \cos \delta & \cos \gamma \sin \delta & -\sin \gamma \cos \delta & -\sin \gamma \sin \delta \\ -\cos \gamma \sin \delta & \cos \gamma \cos \delta & \sin \gamma \sin \delta & -\sin \gamma \cos \delta \\ \sin \gamma \cos \delta & \sin \gamma \sin \delta & \cos \gamma \cos \delta & \cos \gamma \sin \delta \\ -\sin \gamma \sin \delta & \sin \gamma \cos \delta & -\cos \gamma \sin \delta & \cos \gamma \cos \delta \end{bmatrix},$$

respectively.

The aforementioned rotational relationships demonstrate that the 2D SFRFT, GT, and CFRFT can all be regarded as specific geometric transformations in the joint time-frequency domain, thus providing a solid theoretical foundation and practical flexibility for advanced signal analysis in various application scenarios.

2.3. 4D rotation matrix. It has been shown in [26, 65] that any a 4D rotation matrix can be decomposed into the product of two structured matrices associated with quaternion multiplication. This fact can be formally stated as the following proposition.

Proposition 2.6. *Any 4D rotation matrix $\mathbf{Z} \in \mathbb{R}^{4 \times 4}$ can be expressed as the product of two matrices \mathbf{M}_L and \mathbf{M}_R , which correspond to the left-multiplication and right-multiplication by unit quaternions. Specifically, there exist real scalars a, b, c, d, p, q, r, s satisfying $a^2 + b^2 + c^2 + d^2 = 1$, $p^2 + q^2 + r^2 + s^2 = 1$, such that*

$$(2.12) \quad \mathbf{M}_L = \begin{bmatrix} a & -b & -c & -d \\ b & a & -d & c \\ c & d & a & -b \\ d & -c & b & a \end{bmatrix}, \quad \mathbf{M}_R = \begin{bmatrix} p & -q & -r & -s \\ q & p & s & -r \\ r & -s & p & q \\ s & r & -q & p \end{bmatrix},$$

and their product $\mathbf{Z} = \mathbf{M}_L \mathbf{M}_R$ is a valid 4D rotation matrix.

Specifically, the 4D rotation matrices \mathbf{R}_{4D}^S , \mathbf{R}_{4D}^G , and \mathbf{R}_{4D}^C can be obtained by choosing appropriate parameters for \mathbf{M}_L and \mathbf{M}_R as follows:

- For \mathbf{R}_{4D}^S , set $a = \cos \frac{\alpha_1 - \alpha_2}{2}$, $c = \sin \frac{\alpha_1 - \alpha_2}{2}$, $b = d = 0$, and $p = \cos \frac{\alpha_1 + \alpha_2}{2}$, $r = \sin \frac{\alpha_1 + \alpha_2}{2}$, $q = s = 0$;
- For \mathbf{R}_{4D}^G , set $a = \cos \varphi$, $d = \sin \varphi$, $b = c = 0$, and $p = 1$, $q = r = s = 0$;
- For \mathbf{R}_{4D}^C , set $a = \cos \delta$, $b = -\sin \delta$, $c = d = 0$, and $p = \cos \gamma$, $r = \sin \gamma$, $q = s = 0$.

The above fact indicates that the rotational transformations corresponding to the 2D SFRFT, GT, and CFRFT are not general enough. The relationship between them is not inclusive but intersecting, implying that the 2D SFRFT, GT, and CFRFT have their own advantages and disadvantages in practical applications. It is therefore interesting and meaningful to explore a more general rotational transformation to broad the scope of applications. The motivation of this paper is to propose a more general definition of the 2D FRFT, termed the 2D NSFRFT, which has also the rotational transformation relationship with the 2D WD, and the corresponding 4D rotation matrix exhibits a more general form than (2.9)–(2.11).

3. Definition, properties, geometric interpretation and distinctive advantage of the 2D NSFRFT. In this section, we introduce the definition of the 2D NSFRFT, discuss its properties, give its geometric interpretation and highlight its distinctive advantage.

3.1. Definition of the 2D NSFRFT.

Definition 3.1. The 2D NSFRFT of a signal $f(x, y)$ is defined by

$$(3.1) \quad \mathcal{F}_{(a,b,c,d,\theta)}[f](u, v) = F_{(a,b,c,d,\theta)}(u, v) \int_{\mathbb{R}^2} f(x, y) K_{(a,b,c,d,\theta)}(x, y, u, v) dx dy,$$

where

$$(3.2) \quad K_{(a,b,c,d,\theta)}(x, y, u, v) = \frac{1}{2\pi\sqrt{-\mathbf{T}}} e^{\frac{j(p_1 x^2 + p_2 xy + p_3 y^2)}{2\mathbf{T}}} e^{\frac{j(m_1 ux + m_2 vx + m_3 uy + m_4 vy)}{\mathbf{T}}} e^{\frac{j(k_1 u^2 + k_2 uv + k_3 v^2)}{2\mathbf{T}}},$$

and where

$$(3.3) \quad \mathbf{T} = a^2 \sin^2 \theta + b^2 \sin^2 \theta - c^2 \cos^2 \theta - d^2 \cos^2 \theta \neq 0,$$

$$(3.4) \quad \begin{cases} p_1 = \sin \theta \cos \theta - ac + bd, \\ p_2 = -2(bc + ad), \\ p_3 = \sin \theta \cos \theta + ac - bd, \end{cases}$$

$$(3.5) \quad \begin{cases} m_1 = -a \sin \theta + c \cos \theta, \\ m_2 = b \sin \theta + d \cos \theta, \\ m_3 = -b \sin \theta + d \cos \theta, \\ m_4 = -a \sin \theta - c \cos \theta, \end{cases}$$

$$(3.6) \quad \begin{cases} k_1 = \sin \theta \cos \theta - ac - bd, \\ k_2 = 2(bc - ad), \\ k_3 = \sin \theta \cos \theta + ac + bd, \end{cases}$$

$$(3.7) \quad a^2 + b^2 + c^2 + d^2 = 1.$$

In particular, we define that when the parameters $(a, b, c, d, \theta) = (1, 0, 0, 0, 0)$, the corresponding \mathbf{T} becomes zero, and the 2D NSFRFT is specifically defined as the IT, namely,

$$(3.8) \quad \mathcal{F}_{(1,0,0,0,0)}[f](u, v) = F_{(1,0,0,0,0)}(u, v) = f(x, y).$$

It is worth noting that the proposed 2D NSFRFT can be regarded as a special case of the 2D nonseparable linear canonical transform (NSLCT) [38] corresponding to the matrix $\mathbf{X} = [\mathbf{A}, \mathbf{B}; -\mathbf{B}, \mathbf{A}]$, where

$$(3.9) \quad \mathbf{A} = \begin{bmatrix} a \cos \theta - c \sin \theta & b \cos \theta - d \sin \theta \\ -b \cos \theta - d \sin \theta & a \cos \theta + c \sin \theta \end{bmatrix},$$

$$(3.10) \quad \mathbf{B} = \begin{bmatrix} a \sin \theta + c \cos \theta & b \sin \theta + d \cos \theta \\ -b \sin \theta + d \cos \theta & a \sin \theta - c \cos \theta \end{bmatrix}.$$

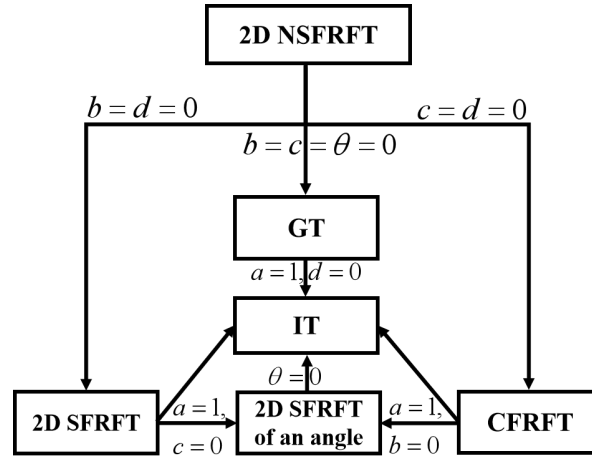


Figure 3.1. Relations between the 2D NSFRFT and its special cases.

Figure 3.1 illustrates the hierarchical relationship between the 2D NSFRFT and its degenerate cases. Specifically, the 2D NSFRFT simplifies to the 2D SFRFT when $b = d = 0$, reduces to the GT when $b = c = \theta = 0$, and reduces to the CFRFT when $c = d = 0$.

Notably, the 2D NSFRFT possesses four independent degrees of freedom, which exceed those of the 2D SFRFT, GT, and CFRFT, enhancing its flexibility in characterizing signal transformations. This parametric richness suggests potential advantages in practical applications such as filtering and image encryption.

In the following, we denote by $P = (a, b, c, d, \theta)$ for convenience. Accordingly, \mathcal{F}_P , $K_P(x, y, u, v)$, $(\mathcal{F}_P)^{-1}$ and F_P denote the 2D NSFRFT operator, the kernel of the 2D NSFRFT, the inverse operator of the 2D NSFRFT and the 2D NSFRFT of f , respectively.

3.2. Properties of the 2D NSFRFT. We discuss some important properties of the 2D NSFRFT, including the inverse formula, time translation and frequency modulation properties, the orthogonality of kernel functions, the energy conservation property, and the relationship with the 2D WD.

3.2.1. Inverse formula. The inverse formula of the 2D NSFRFT of $f(x, y)$ is

$$(3.11) \quad f(x, y) = \int_{\mathbb{R}^2} F_P(u, v) K_P^*(x, y, u, v) du dv.$$

3.2.2. Time translation property.

$$(3.12) \quad \mathcal{F}_P[\mathcal{T}_{\tau, \eta}[f]](u, v) = e^{js'u} e^{jt'v} \mathcal{F}_P[f](u', v'),$$

where $\mathcal{T}_{\tau, \eta}$ denotes the time translation operator defined by $\mathcal{T}_{\tau, \eta}[f](x, y) = f(x - \tau, y - \eta)$, and $s' = l_\theta(-c, a)\tau + l_\theta(-d, b)\eta$, $t' = l_\theta(-d, -b)\tau + l_\theta(c, a)\eta$, $u' = u - l_\theta(a, c)\tau - l_\theta(b, d)\eta$, $v' = v - l_\theta(-b, d)\tau - l_\theta(a, -c)\eta$, and where $l_\theta(m, n) = m \cos \theta - n \sin \theta$.

3.2.3. Frequency modulation property.

$$(3.13) \quad \mathcal{F}_P[\mathcal{M}_{n_1, n_2}[f]](u, v) = e^{js''u} e^{jt''v} \mathcal{F}_P[f](u'', v''),$$

where \mathcal{M}_{n_1, n_2} denotes the frequency modulation operator defined by $\mathcal{M}_{n_1, n_2}[f](x, y) = e^{jn_1 x} \times e^{jn_2 y} f(x, y)$, and $s'' = l_\theta(a, c)n_1 + l_\theta(b, d)n_2$, $t'' = l_\theta(-b, d)n_1 + l_\theta(a, -c)n_2$, $u'' = u - l_\theta(c, -a)n_1 - l_\theta(d, -b)n_2$, $v'' = v - l_\theta(d, b)n_1 - l_\theta(-c, -a)n_2$.

3.2.4. Orthogonality of kernel functions.

$$(3.14) \quad \int_{\mathbb{R}^2} K_P(x, y, u, v) K_P^*(x, y, \hat{u}, \hat{v}) dx dy = \delta(u - \hat{u}, v - \hat{v}).$$

3.2.5. Energy conservation property.

$$(3.15) \quad \int_{\mathbb{R}^2} |f(x, y)|^2 dx dy = \int_{\mathbb{R}^2} |F_P(u, v)|^2 du dv.$$

3.2.6. Relationship with the 2D WD.

$$(3.16) \quad W_{F_P}(x, y, u, v) = W_f(\tilde{x}, \tilde{y}, \tilde{u}, \tilde{v}),$$

where $\tilde{x} = l_\theta(a, c)x + l_\theta(-b, d)y + l_\theta(-c, a)u + l_\theta(-d, -b)v$, $\tilde{y} = l_\theta(b, d)x + l_\theta(a, -c)y + l_\theta(-d, b)u + l_\theta(c, a)v$, $\tilde{u} = l_\theta(c, -a)x + l_\theta(d, b)y + l_\theta(a, c)u + l_\theta(-b, d)v$, $\tilde{v} = l_\theta(d, -b)x + l_\theta(-c, -a)y + l_\theta(b, d)u + l_\theta(a, -c)v$.

The proofs of these properties are similar to those of the 1D FRFT, so they are omitted here.

3.3. Geometric interpretation of the 2D NSFRFT. From (3.16), we can conclude that the 2D WD W_{F_P} of the 2D NSFRFT F_P of a 2D function f can be obtained by applying a 4D linear transformation to the 2D WD W_f of f , using the transformation matrix

$$(3.17) \quad \mathbf{R}_{4D}^{NS} = \begin{bmatrix} a \cos \theta - c \sin \theta & -b \cos \theta - d \sin \theta & -a \sin \theta - c \cos \theta & b \sin \theta - d \cos \theta \\ b \cos \theta - d \sin \theta & a \cos \theta + c \sin \theta & -b \sin \theta - d \cos \theta & -a \sin \theta + c \cos \theta \\ a \sin \theta + c \cos \theta & -b \sin \theta + d \cos \theta & a \cos \theta - c \sin \theta & -b \cos \theta - d \sin \theta \\ b \sin \theta + d \cos \theta & a \sin \theta - c \cos \theta & b \cos \theta - d \sin \theta & a \cos \theta + c \sin \theta \end{bmatrix}.$$

Furthermore, according to Proposition 2.6, it can be verified that \mathbf{R}_{4D}^{NS} is a specific 4D rotation matrix. This confirms that the proposed 2D NSFRFT preserves the energy and symplectic structure of the WD. Moreover, the matrix \mathbf{R}_{4D}^{NS} provides a unified representation that includes the classical forms \mathbf{R}_{4D}^S , \mathbf{R}_{4D}^G , and \mathbf{R}_{4D}^C as special cases. Consequently, the 2D NSFRFT generalizes the 2D SFRFT, GT, and CFRFT, offering greater flexibility and broader potential in fractional signal processing applications.

3.4. Unique advantage of the 2D NSFRFT: handling specific 2D chirp signals with nonseparable terms. In practical applications such as radar, communication, sonar, and optical imaging, in which 2D chirp signals with nonseparable terms frequently arise. These nonseparable terms reflect coupled modulations along the two spatial axes, posing significant challenges for conventional time-frequency analysis methods.

Although the 2D SFRFT, GT, and CFRFT provide various rotational mechanisms in the joint time-frequency domain, they are inherently limited when dealing with 2D signals containing nonseparable quadratic phase couplings. Specifically, the separable structure of the 2D SFRFT and the particular rotation plane of the GT and CFRFT cannot fully align or focus such nonseparable structures. In contrast, the proposed 2D NSFRFT incorporates nonseparable terms in its kernel function, enabling it to effectively process 2D chirp signals with nonseparable terms. This capability makes the 2D NSFRFT particularly advantageous for applications in weak signal detection, interference suppression, filtering, and enhanced time-frequency feature extraction.

A rigorous mathematical proof demonstrating the ability of the 2D NSFRFT to process a specific class of 2D chirp signals with nonseparable terms is provided in Appendix A. Its capability to handle such signals stems from the fact that they can form impulses in the corresponding 2D NSFRFT domain, which distinguishes it from existing 2D FRFTs.

4. Discrete algorithms of the 2D NSFRFT. In this section, we present three discrete implementations of the 2D NSFRFT: a direct method offering high accuracy but with high computational cost, and two fast algorithms derived from matrix decomposition frameworks adapted for the 2D NSFRFT. Additionally, we compare the performance of these methods.

4.1. The direct method. The most straightforward way to implement the discrete 2D NSFRFT is by discretizing its continuous version in (3.1) through direct sampling and summation:

$$(4.1) \quad F_P(p\Delta_u, q\Delta_v) = \frac{1}{2\pi\sqrt{-\mathbf{T}}} e^{\frac{j(k_1 p^2 \Delta_u^2 + k_2 p q \Delta_u \Delta_v + k_3 q^2 \Delta_v^2)}{2\mathbf{T}}} \sum_m \sum_n f(m\Delta_x, n\Delta_y) \Delta_x \Delta_y \\ \times e^{\frac{j(p_1 m^2 \Delta_x^2 + p_2 m n \Delta_x \Delta_y + p_3 n^2 \Delta_y^2)}{2\mathbf{T}}} e^{\frac{j(m_1 p \Delta_u + m_2 q \Delta_v) m \Delta_x + j(m_3 p \Delta_u + m_4 q \Delta_v) n \Delta_y}{\mathbf{T}}},$$

where Δ_x and Δ_y denote the input sampling intervals and Δ_u and Δ_v denote the output sampling intervals.

This method is intuitive and accurate, as it directly samples the continuous version. However, its computational complexity $O(N^4)$ scales poorly with data size, making it impractical for large-scale signal or image processing. As such, it serves primarily as a benchmark for evaluating the accuracy of more efficient implementations [8, 16, 32, 38, 40, 56].

4.2. Fast implementations based on 2D NSLCT decomposition. We propose two fast algorithms for the 2D NSFRFT by adapting matrix decomposition strategies from the 2D NSLCT in order to address the high computational cost of the direct method. Specifically, by substituting the transformation matrices in existing NSLCT decomposition frameworks with those defined by (3.9) and (3.10), the 2D NSFRFT can be efficiently realized through a cascade of low-complexity 2D discrete operators.

The decomposition framework involves operators such as 2D chirp multiplications (CM), chirp convolutions (CC), FTs, and affine transforms (AT), whose definitions and computational complexity can be found in [8, 16, 40, 56] and are not repeated here.

The first fast algorithm (Algorithm I) includes a 2D AT and thus requires interpolation, while the second (Algorithm II) avoids interpolation by employing only 2D CM and CC operations, resulting in higher accuracy. A summary of their decomposition forms, operator sequences, and computational complexities is provided in Table 4.1. Detailed parameter selection strategies and conditions are available in [40, 56].

Table 4.1
Comparison between Algorithms I and II

Algorithm	Matrix Decomposition	Operator Form	Computational Complexity	Reference
Algorithm I	$\underbrace{\begin{bmatrix} \mathbf{I} & \mathbf{0} \\ \mathbf{AB}^{-1} & \mathbf{I} \end{bmatrix}}_{2\text{D CM}} \underbrace{\begin{bmatrix} \mathbf{0} & \mathbf{I} \\ -\mathbf{I} & \mathbf{0} \end{bmatrix}}_{2\text{D FT}} \underbrace{\begin{bmatrix} (\mathbf{B}^T)^{-1} & \mathbf{0} \\ \mathbf{0} & \mathbf{B} \end{bmatrix}}_{2\text{D AT}} \underbrace{\begin{bmatrix} \mathbf{I} & \mathbf{0} \\ \mathbf{B}^{-1}\mathbf{A} & \mathbf{I} \end{bmatrix}}_{2\text{D CM}}$	$\mathcal{O}_{\text{CM}}^{\mathbf{AB}^{-1}} \mathcal{F}_{x,y} \mathcal{O}_{\text{AT}}^{\mathbf{B}} \mathcal{O}_{\text{CM}}^{\mathbf{B}^{-1}\mathbf{A}}$	$O(N^2 \log N)$	[56]
Algorithm II-1 ($\mathbf{B} = \mathbf{B}^T$)	$\underbrace{\begin{bmatrix} \mathbf{I} & \mathbf{0} \\ (\mathbf{A} - \mathbf{I})\mathbf{B}^{-1} & \mathbf{I} \end{bmatrix}}_{2\text{D CM}} \underbrace{\begin{bmatrix} \mathbf{I} & \mathbf{B} \\ \mathbf{0} & \mathbf{I} \end{bmatrix}}_{2\text{D CC}} \underbrace{\begin{bmatrix} \mathbf{I} & \mathbf{0} \\ \mathbf{B}^{-1}(\mathbf{A} - \mathbf{I}) & \mathbf{I} \end{bmatrix}}_{2\text{D CM}}$	$\mathcal{O}_{\text{CM}}^{(\mathbf{A}-\mathbf{I})\mathbf{B}^{-1}} \mathcal{O}_{\text{CC}}^{\mathbf{B}} \mathcal{O}_{\text{CM}}^{\mathbf{B}^{-1}(\mathbf{A}-\mathbf{I})}$	$O(N^2 \log N)$	[40]
Algorithm II-2 ($\mathbf{B} \neq \mathbf{B}^T$)	$\underbrace{\begin{bmatrix} \mathbf{I} & \mathbf{0} \\ (\mathbf{D}' - \mathbf{I})\mathbf{B}'^{-1} & \mathbf{I} \end{bmatrix}}_{2\text{D CM}} \underbrace{\begin{bmatrix} \mathbf{I} & \mathbf{B}' \\ \mathbf{0} & \mathbf{I} \end{bmatrix}}_{2\text{D CC}} \underbrace{\begin{bmatrix} \mathbf{I} & \mathbf{0} \\ \mathbf{B}'^{-1}(\mathbf{A}' - \mathbf{I}) & \mathbf{I} \end{bmatrix}}_{2\text{D CM}} \underbrace{\begin{bmatrix} \mathbf{I} & \mathbf{H} \\ \mathbf{0} & \mathbf{I} \end{bmatrix}}_{2\text{D CC}}$	$\mathcal{O}_{\text{CM}}^{(\mathbf{D}'-\mathbf{I})\mathbf{B}'^{-1}} \mathcal{O}_{\text{CC}}^{\mathbf{B}'} \mathcal{O}_{\text{CM}}^{\mathbf{B}'^{-1}(\mathbf{A}'-\mathbf{I})} \mathcal{O}_{\text{CC}}^{\mathbf{H}}$	$O(N^2 \log N)$	[40]

4.3. Comparisons between the two fast algorithms and the direct method. In this part, we compare the two fast algorithms with the direct method in terms of computational complexity, accuracy, and reversibility. The direct method introduced in Part A serves as a benchmark for accuracy evaluation. To this end, we perform simulations using different input functions and parameter matrices \mathbf{X} to assess the effectiveness of the three algorithms in computing the 2D NSFRFT.

Specifically, two representative 2D Hermite-Gaussian functions are chosen as test signals due to their diversity and analytical tractability. The first is the second-order function $g_1 = 4e^{-\frac{x^2+y^2}{2}}(4x^2y^2 - 2(x^2 + y^2) + 1)$; the second is a combination of basis functions, $g_2 = \Psi_{1,2}(x, y) + \Psi_{3,1}(x, y)$, where $\Psi_{m,n}(x, y) = \psi_m(x)\psi_n(y)$ and $\psi_m(x)$ is the 1D m -th order Hermite-Gaussian function defined by

$$(4.2) \quad \psi_m(x) = \frac{1}{\sqrt{2^m m! \sqrt{\pi}}} e^{-x^2/2} H_m(x),$$

with $H_m(x)$ denoting the Hermite polynomial. The normalized mean square error (NMSE) is used to quantify the accuracy of the results.

4.3.1. Computational complexity. The computational complexity of two fast algorithms is summarized in Table 4.1; see also [8, 16, 40, 56] for details on the underlying 2D discrete operators.

4.3.2. Accuracy simulation for various input functions. We evaluate the accuracy and efficiency of the two fast algorithms using different input functions, with the parameter matrix fixed as \mathbf{X}_{ac1} . Accuracy is measured by the NMSE, defined by

$$(4.3) \quad \text{NMSE}_{ac} = \frac{\sum_p \sum_q |G(p\Delta_u, q\Delta_v) - G_0(p\Delta_u, q\Delta_v)|^2}{\sum_p \sum_q |G_0(p\Delta_u, q\Delta_v)|^2},$$

where G denotes the output of Algorithm I or II and G_0 is the result of the direct method.

The parameter set used in the 2D NSFRFT numerical simulations is $P = (0.4033, 0.1555, 0.2851, -0.8555, \frac{\pi}{8})$, so the corresponding parameter matrix \mathbf{X}_{ac1} is

$$(4.4) \quad \mathbf{X}_{ac1} = \begin{bmatrix} 0.2635 & 0.4710 & 0.4177 & -0.7309 \\ 0.1837 & 0.4817 & -0.8499 & -0.1091 \\ -0.4177 & 0.7309 & 0.2635 & 0.4710 \\ 0.8499 & 0.1091 & 0.1837 & 0.4817 \end{bmatrix}.$$

Figure 4.1 shows the simulation results of the 2D NSFRFT. Figure 4.1(a) displays the input function g_1 , while (b)–(d) present the outputs of the direct method, Algorithm I, and Algorithm II, respectively. All methods use $\Delta_x = \Delta_y = \Delta_u = \Delta_v = 0.1772$ with $M = N = 200$ sampling points.

Figure 4.1 confirms that both fast algorithms achieve results comparable to the direct method. Table 4.2 further shows that they offer significant speed improvements, with Algorithm II achieving the highest accuracy.

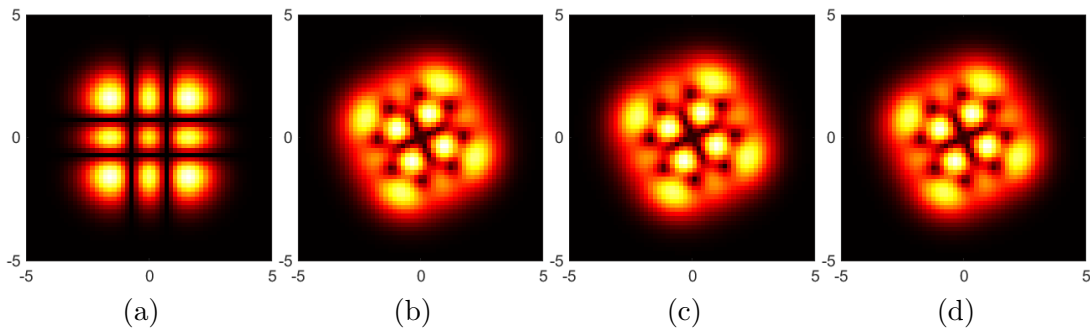


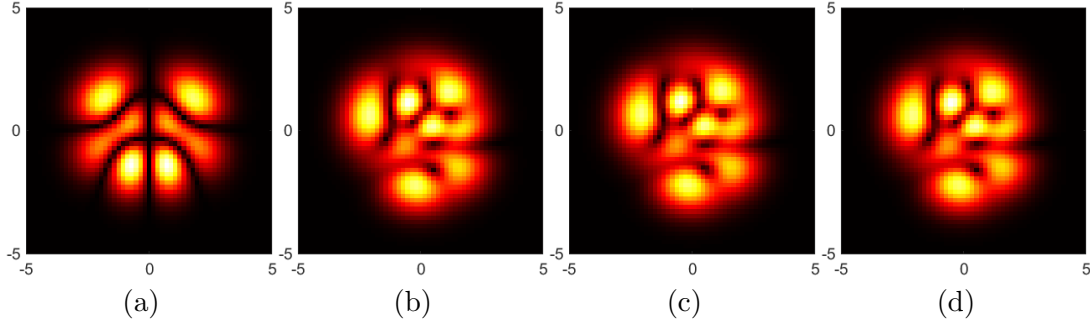
Figure 4.1. 2D NSFRFT under the condition of input function g_1 and parameter matrix \mathbf{X}_{ac1} .

In the second simulation, the input function is changed to g_2 while keeping \mathbf{X}_{ac1} unchanged. As shown in Figure 4.2 and Table 4.3, the results are consistent with the previous case: both fast algorithms significantly reduce computation time, and Algorithm II achieves the best accuracy.

Table 4.2

The numerical calculation time and accuracy of the three methods under g_1 and \mathbf{X}_{ac1}

	Direct method	Algorithm I	Algorithm II
Time	166.1043s	0.0101s	0.0068s
NMSE	/	2.2293×10^{-3}	3.6689×10^{-8}

**Figure 4.2.** 2D NSFRFT under the condition of input function g_2 and parameter matrix \mathbf{X}_{ac1} .**Table 4.3**

The numerical calculation time and accuracy of the three methods under g_2 and \mathbf{X}_{ac1}

	Direct method	Algorithm I	Algorithm II
Time	162.1484s	0.0080s	0.0078s
NMSE	/	2.2407×10^{-3}	3.3724×10^{-8}

4.3.3. Accuracy simulation for different parameter matrices. We conduct a new round of numerical simulation comparison experiments by changing different parameter matrices. The input function is still g_1 and a new parameter set $P = (0.1745, 0.5951, -0.7329, 0.2798, \frac{\pi}{9})$, yielding the matrix

$$(4.5) \quad \mathbf{X}_{ac2} = \begin{bmatrix} 0.4146 & 0.4635 & -0.6291 & 0.4664 \\ -0.6549 & -0.0867 & 0.0594 & 0.7484 \\ 0.6291 & -0.4664 & 0.4146 & 0.4635 \\ -0.0594 & -0.7484 & -0.6549 & -0.0867 \end{bmatrix}.$$

The simulation results are shown in Figure 4.3, and the corresponding time and NMSE values are listed in Table 4.4. As before, both fast algorithms significantly outperform the direct method in efficiency, with Algorithm II again achieving superior accuracy.

From the results of the three experiments, it can be concluded that the proposed two algorithms are highly efficient and exhibit satisfactory accuracy.

4.3.4. Reversibility. Reversibility is a fundamental property of the 2D NSFRFT and underpins many of its applications. To evaluate this, we conduct a simulation using the input

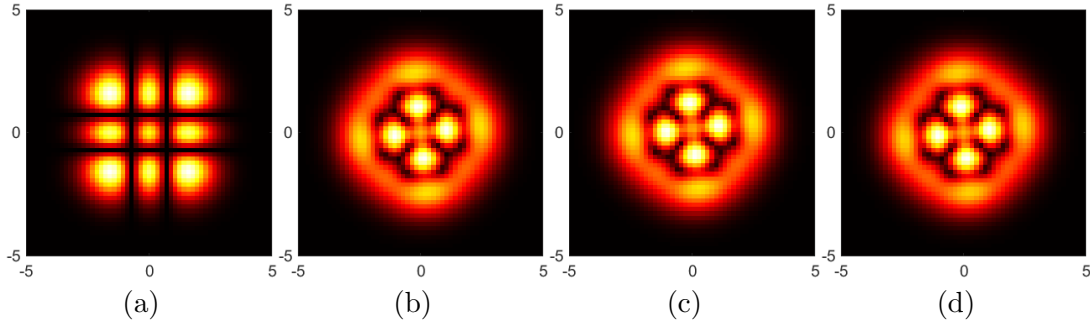


Figure 4.3. 2D NSFRFT under the condition of input function g_1 and parameter matrix \mathbf{X}_{ac2} .

Table 4.4

The numerical calculation time and accuracy of the three methods under g_1 and \mathbf{X}_{ac2}

	Direct method	Algorithm I	Algorithm II
Time	163.5826s	0.0090s	0.0059s
NMSE	/	2.5662×10^{-2}	3.671×10^{-8}

function g_2 and the parameter set $P = (-0.1601, 0.6966, 0.2625, 0.6483, \frac{\pi}{6})$, yielding the matrix

$$(4.6) \quad \mathbf{X}_{re} = \begin{bmatrix} -0.2699 & 0.2791 & 0.1473 & 0.9097 \\ -0.9274 & -0.0074 & 0.2131 & -0.3074 \\ -0.1473 & -0.9097 & -0.2699 & 0.2791 \\ -0.2131 & 0.3074 & -0.9274 & -0.0074 \end{bmatrix}.$$

Reversibility is assessed by computing the NMSE between the original signal g and its reconstruction g' obtained through forward and inverse 2D NSFRFT:

$$(4.7) \quad \text{NMSE}_{re} = \frac{\sum_m \sum_n |g'(m\Delta_x, n\Delta_y) - g(m\Delta_x, n\Delta_y)|^2}{\sum_m \sum_n |g(m\Delta_x, n\Delta_y)|^2},$$

where $g'(x, y) = (\mathcal{F}_P)^{-1}[\mathcal{F}_P[g]](x, y)$.

Figure 4.4 presents the reversibility simulation results for g_2 , while Table 4.5 summarizes the corresponding computation time and NMSE values. Both Algorithms I and II effectively preserve reversibility with significantly reduced computation time compared to the direct method. Notably, Algorithm II achieves the highest accuracy, confirming its superior performance in reversible 2D NSFRFT implementation.

The four simulations collectively highlight the advantages of the proposed algorithms, which exhibit both high computational efficiency and accuracy. In particular, for applications requiring reversibility, the fast algorithms achieve superior performance in terms of both precision and speed.

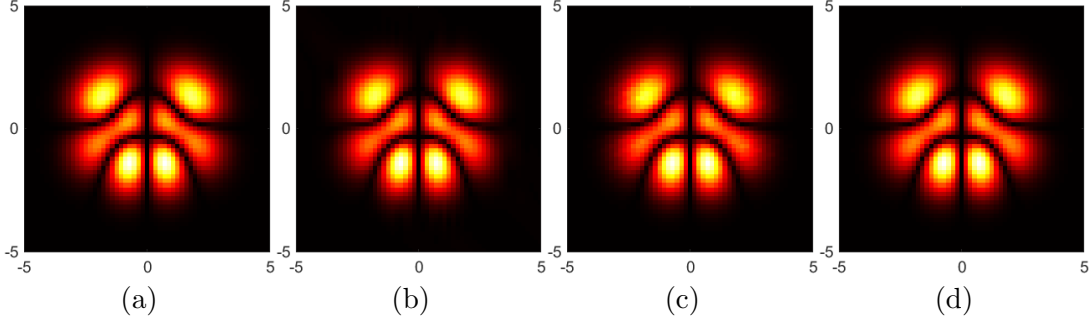


Figure 4.4. The reversibility of the 2D NSFRFT under the condition of input function g_2 and parameter matrix \mathbf{X}_{re} .

Table 4.5

The numerical calculation time and accuracy of the reversibility experiment under g_2 and \mathbf{X}_{re} by three methods

	Direct method	Algorithm I	Algorithm II
Time	328.7254s	0.0729s	0.0250s
NMSE	6.8233×10^{-1}	4.6038×10^{-3}	7.989×10^{-31}

5. Applications. Since the 2D NSFRFT extends the 2D SFRFT, many applications of the latter can be generalized to the former. This section explores several applications of the 2D NSFRFT, including image encryption, decryption, and optimal filter design. Additionally, we also leverage the distinct advantage of the 2D NSFRFT to design bandpass and bandstop filters.

5.1. Double random phase encryption and decryption (DRPED). The 2D SFRFT has been widely used in image encryption and decryption [12, 15, 19, 20, 50, 53, 55]. Compared to the separable case with two degrees of freedom, the 2D NSFRFT offers enhanced security with four degrees of freedom, while maintaining comparable computational complexity ($O(N^2 \log N)$). In the following, the DRPED method is extended to the 2D NSFRFT domain, as illustrated in Figure 5.1.

We conduct a simulation experiment to verify the correctness and effectiveness of the proposed method. The input is a 256×256 medical image containing multiple subpleural plaques and nodules, as shown in Figure 5.2(a). Two random phase masks, D1 and D2, are generated using random numbers. The parameters of the 2D NSFRFT are set to $(0.7548, 0.4147, -0.0442, -0.5063, \frac{\pi}{3})$, and the corresponding encrypted image is shown in Figure 5.2(b). During decryption, when all keys are correctly specified, the original image is successfully recovered, as illustrated in Figure 5.2(c); otherwise, incorrect keys fail to produce a valid reconstruction, as shown in Figure 5.2(d).

In addition, the mean squared error (MSE) is used to evaluate the difference between the

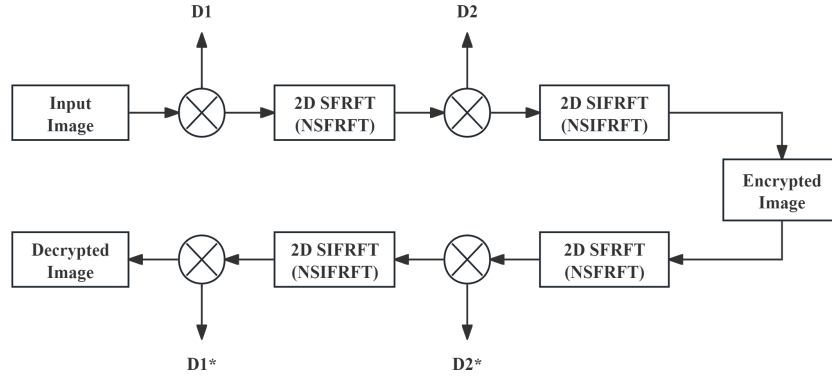


Figure 5.1. DRPED algorithms based on the 2D SFRFT and NSFRFT. $D1$ and $D2$ denote two random phase masks, 2D SIFRFT and 2D NSIFRFT denote the 2D separable inverse FRFT and nonseparable inverse FRFT, respectively.

input and decrypted images, defined by

$$(5.1) \quad \text{MSE} = \frac{\sum \sum (|\text{Decrypted image}| - |\text{Input image}|)^2}{M \times N},$$

where $M \times N$ denotes the image size. When all parameters set correctly, the calculated MSE is 8.3345×10^{-26} , indicating that the image is perfectly recovered.

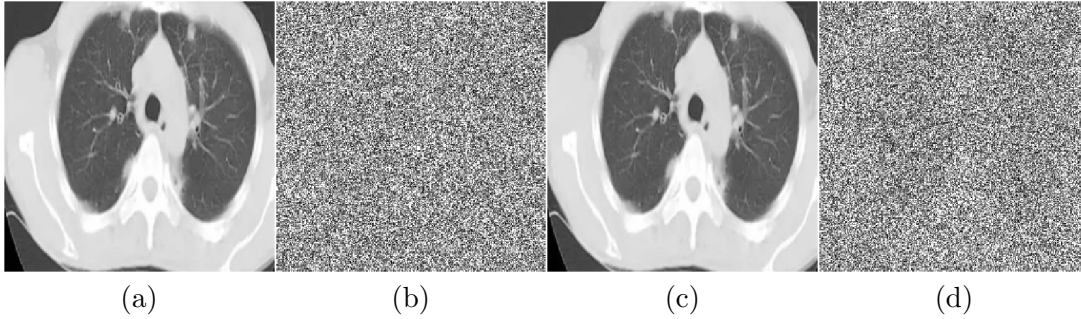


Figure 5.2. Simulation results for DRPED method based on 2D NSFRFT. (a) The input image, (b) The encrypted image, (c) The decrypted image decrypted with the correct keys $P = (0.7548, 0.4147, -0.0442, -0.5063, \frac{\pi}{3})$, (d) The decrypted image with wrong keys $P = (\frac{1}{2}, \frac{1}{2}, \frac{1}{2}, \frac{1}{2}, \frac{\pi}{5})$.

Next, we conduct a perturbation experiment to further evaluate the sensitivity of the proposed encryption method with respect to parameters of the 2D NSFRFT. While keeping the parameters $(a, b, c, d) = (0.7548, 0.4147, -0.0442, -0.5063)$ fixed, a perturbation δ is added to the parameter $\theta = \frac{\pi}{3}$, with δ ranging from -0.5 to 0.5 in steps of 0.05 . The MSE between the input and decrypted images is recorded for each perturbation value. As shown in Figure 5.3, the MSE increases sharply as δ changes, and even small perturbations result in significant

distortion of the decrypted image. This demonstrates that the proposed encryption system is highly sensitive to the 2D NSFRFT parameters, thereby ensuring strong security.

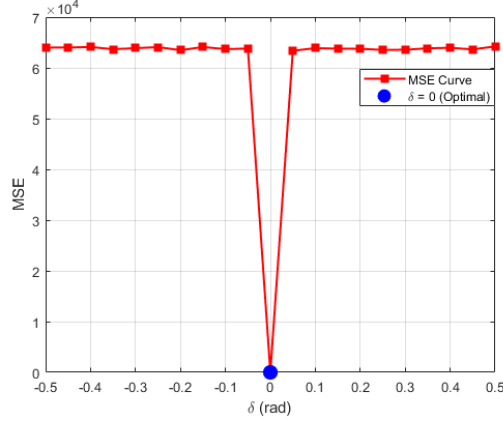


Figure 5.3. Curves of the MSE values between the decrypted image and the input image when δ changes.

5.2. Filter design. The multiplicative filter in the 2D NSFRFT domain is defined by

$$(5.2) \quad \hat{f}(x, y) = (\mathcal{F}_P)^{-1} [H(u, v) \mathcal{F}_P[f]](x, y),$$

where $H(u, v)$ denotes the filter transfer function.

In this paper, we explore two filtering strategies in the 2D NSFRFT domain: optimal filtering and passband and stopband filtering, the latter leveraging the structural advantages of the 2D NSFRFT.

5.2.1. Optimal filter. We begin with the optimal filtering approach. Considering the signal observation model $f(x, y) = g(x, y) + n(x, y)$, where $g(x, y)$ is the desired signal and $n(x, y)$ denotes additive noise. The objective is to recover $g(x, y)$ as accurately as possible. The following correlation functions are assumed to be known:

- The cross-correlation $R_{gf}(x, y, \sigma, \tau)$ between $g(x, y)$ and $f(x, y)$;
- The auto-correlation $R_{gg}(x, y, \sigma, \tau)$ of $g(x, y)$;
- The auto-correlation $R_{ff}(x, y, \sigma, \tau)$ of $f(x, y)$.

Since the 2D NSFRFT is an orthonormal transform, the optimal filter in the NSFRFT domain is similar to that in the 2D SFRFT domain [18]. The corresponding filter transfer function is given by

$$(5.3) \quad H_{\text{opt}}(u, v) = \frac{R_{G_P F_P}(u, v, u, v)}{R_{F_P F_P}(u, v, u, v)},$$

where $R_{G_P F_P}$ and $R_{F_P F_P}$ denote the cross-correlation and auto-correlation functions in the 2D NSFRFT domain, respectively, defined by

$$(5.4) \quad R_{G_P F_P}(u, v, u, v) = \int_{\mathbb{R}^4} K_P(x, y, u, v) K_P^*(\sigma, \tau, u, v) R_{gf}(x, y, \sigma, \tau) dx dy d\sigma d\tau,$$

$$(5.5) \quad R_{F_P F_P}(u, v, u, v) = \int_{\mathbb{R}^4} K_P(x, y, u, v) K_P^*(\sigma, \tau, u, v) R_{ff}(x, y, \sigma, \tau) dx dy d\sigma d\tau.$$

and the MSE for the optimal filter is

$$(5.6) \quad \text{MSE} = \int_{\mathbb{R}^2} R_{G_P G_P}(u, v, u, v) - 2 \operatorname{Re} (H_{\text{opt}}^*(u, v) R_{F_P G_P}(u, v, u, v)) \\ + |H_{\text{opt}}(u, v)|^2 R_{F_P F_P}(u, v, u, v) du dv,$$

where

$$(5.7) \quad R_{G_P G_P}(u, v, u, v) = \int_{\mathbb{R}^4} K_P(x, y, u, v) K_P^*(\sigma, \tau, u, v) R_{gg}(x, y, \sigma, \tau) dx dy d\sigma d\tau$$

(5.3) provides the basis for constructing the optimal filter under a given parameter set $P = (a, b, c, d, \theta)$, while (5.6) defines the associated MSE to be minimized.

The overall design procedure is summarized in Algorithm 5.1. In practice, we employ the genetic algorithm (GA) to globally search for the optimal parameter set $P_{\text{opt}} = (a, b, c, d, \theta)_{\text{opt}}$ that minimizes the MSE in (5.6). The GA-based approach offers enhanced robustness against local minima and improved convergence performance.

Algorithm 5.1 Optimal filter design in the 2D NSFRFT domain

Require: Observed signal $f(x, y)$, known correlation functions R_{gf}, R_{gg}, R_{ff}

Ensure: Optimal filter $H_{\text{opt}}(u, v)$ and optimal parameter set $P_{\text{opt}} = (a, b, c, d, \theta)_{\text{opt}}$

```

1: for each candidate parameter set  $P = (a, b, c, d, \theta)$  do
2:   Compute 2D NSFRFT kernel  $K_P(x, y, u, v)$ 
3:   Calculate correlation functions and construct  $H_{\text{opt}}(u, v)$  using (5.3)–(5.5)
4:   Evaluate MSE using (5.6)
5:   if current MSE < minimum recorded MSE then
6:     Update  $P_{\text{opt}} \leftarrow P$ 
7:     Store current  $H_{\text{opt}}(u, v)$ 
8:   end if
9: end for
10: return  $H_{\text{opt}}(u, v)$ ,  $P_{\text{opt}}$ , MSE

```

In the following, we consider three types of experiments to comprehensively evaluate the denoising capability of the 2D NSFRFT-based optimal filtering method:

- Synthetic Gaussian signals;
- Simulated Newton fringe pattern denoising;
- Real-world image denoising.

The filtering performance in the 2D NSFRFT domain is compared with that in the 2D FT, 2D SFRFT, GT, and CFRFT domains using MSE (The MSE has been converted to logarithmic scale with base 10 for the convenience of observation and comparison.), structural similarity index measure (SSIM), and peak signal-to-noise ratio (PSNR) as evaluation metrics. A smaller MSE indicates higher accuracy. A higher SSIM value closer to 1 indicates better filtering quality, while a larger PSNR value corresponds to less distortion. In particular, the simulation results demonstrate the correctness and effectiveness of the optimal filtering in the 2D NSFRFT domain.

(1) Synthetic Gaussian signals

In this experiment, we utilize two 2D Gaussian signals as inputs: $g_1(x, y) = e^{-(x^2+y^2)}$, which does not contain nonseparable term, and $g_2(x, y) = e^{-(x^2+1.5xy+y^2)}$, which includes nonseparable term. Both signals are corrupted by white Gaussian noise, and the proposed optimal filtering method is applied to restore the original signals by removing the noise.

The results of the optimal filtering in different transform domains, under various signal-to-noise ratios (SNRs), are summarized in Table 5.1 for g_1 and Table 5.2 for g_2 . These tables present the MSE and PSNR values, along with the corresponding optimal parameters for each transform domain. As shown in both tables, the optimal filter in the 2D NSFRFT domain consistently outperforms those in the 2D FT, 2D SFRFT, GT, and CFRFT domains, achieving lower MSE and higher PSNR values. This confirms the superior performance of the 2D NSFRFT-based optimal filter in denoising synthetic Gaussian signals, irrespective of the presence of nonseparable terms.

Table 5.1

Optimal filtering performance for g_1 in different transform domains under various SNRs

Transform	SNR						
	MSE / PSNR (Optimal parameters)						
	-15	-10	-5	0	5	10	15
FT	-3.4353/34.3586	-3.7328/37.3480	-4.0858/40.9039	-4.4749/44.8011	-4.8870/48.8938	-5.3140/53.1459	-5.7541/57.5504
2D SFRFT	-3.8918/40.6031 (0.0182, -3.1234)	-4.2336/43.6547 (-0.0182, 3.1234)	-4.6013/47.1122 (0.0182, -3.1234)	-4.9589/50.2362 (-0.0126, 3.1290)	-5.3797/54.5295 (-0.0199, 0.0199)	-5.8127/58.7046 (-0.0169, 0.0169)	-6.2568/64.0169 (-0.0731, 0.0731)
GT	-3.8331/41.2619 (0.0755)	-4.1792/44.0800 (-0.0629)	-4.5579/47.4684 (-0.0619)	-4.9581/49.9247 (0.0005)	-5.3788/54.1122 (0.0002)	-5.8122/58.4178 (-0.0007)	-6.2560/62.7937 (-0.0010)
CFRFT	-3.8278/39.0811 (-2.6833, 2.6779)	-4.1785/44.1336 (1.2614, -1.0307)	-4.5534/45.9228 (2.0792, -2.0796)	-4.9064/49.8208 (1.7481, -2.3325)	-5.3482/54.6990 (1.4409, -1.7960)	-5.8318/59.5837 (-0.4212, 0.5674)	-6.2724/63.8273 (0.2855, -0.2082)
2D NSFRFT	-4.0156/42.2726 (-0.0029, -0.0068, 0.0008, 0.9999, 1.5774)	-4.2940/44.2647 (0.0059, -0.0056, -0.0037, 0.9999, 4.7181)	-4.8726/49.9987 (-0.0483, 0.0006, -0.9979, -0.0442, 4.7329)	-5.0204/50.9161 (0.0000, 0.0000, -0.9999, 0.0029, 4.6973)	-5.4116/55.5659 (0.1087, 0.0417, 0.0487, 0.9920, 1.4767)	-5.8449/59.7583 (0.1092, 0.0413, 0.0488, 0.9920, 1.4768)	-6.2762/64.2091 (0.9401, -0.3196, 0.1181, 0.0078, 6.2832)

Table 5.2

Optimal filtering performance for g_2 in different transform domains under various SNRs

Transform	SNR						
	MSE / PSNR (Optimal parameters)						
	-15	-10	-5	0	5	10	15
FT	-3.3981/33.9949	-3.7100/37.1453	-4.0643/40.7306	-4.4554/44.6337	-4.8721/48.7444	-5.3038/53.0488	-5.7449/57.4687
2D SFRFT	-3.5313/36.6216 (0.2841, -0.2841)	-3.8531/39.8226 (0.2808, -0.2808)	-4.2173/43.4839 (-0.2670, 0.2670)	-4.6215/47.5699 (0.2420, -0.2420)	-5.0483/51.7635 (0.2395, -0.2395)	-5.4855/56.0606 (-0.2360, 0.2360)	-5.9309/60.4652 (-0.2295, 0.2295)
GT	-3.4985/35.8262 (-0.0005)	-3.8308/38.9588 (-0.0010)	-4.2034/42.5642 (-0.0011)	-4.6034/47.9651 (0.0760)	-5.0256/51.8688 (0.0775)	-5.4600/55.9760 (0.0784)	-5.9050/60.1697 (0.0713)
CFRFT	-3.5290/37.4070 (-0.2025, 0.2766)	-3.8589/40.0224 (0.2597, -0.1859)	-4.2309/43.5807 (0.2599, -0.1861)	-4.6261/47.5823 (0.2565, -0.1474)	-5.0433/51.6072 (0.2531, -0.1457)	-5.4730/55.6951 (0.2220, -0.1304)	-5.9162/60.0184 (0.2477, -0.1431)
2D NSFRFT	-3.8160/38.5729 (-0.7117, 0.0033, 0.0207, -0.7021, 2.3912)	-4.1812/42.1354 (-0.0797, 0.6987, -0.7059, 0.0846, 3.9318)	-4.5447/46.1486 (-0.0550, 0.6788, -0.7319, -0.0227, 4.0098)	-4.9270/49.6359 (-0.1536, 0.6829, -0.6916, 0.1780, 3.9132)	-5.3661/54.2214 (-0.0680, 0.6652, -0.7430, -0.0277, 4.0036)	-5.7803/58.4129 (-0.1954, 0.6050, -0.7584, 0.1435, 4.0417)	-6.2273/62.8833 (-0.1627, 0.6338, -0.7417, 0.1474, 4.0633)

(2) Simulated Newton fringe pattern denoising

Newton rings, or Newton fringe patterns [21–23, 58], are a type of interference pattern typically observed in thin films, where concentric rings of varying brightness are formed due to the constructive and destructive interference of light. The intensity distribution of the Newton rings can be described as $I(x, y) = I_0 + A \cos[\varphi(x, y)]$, where I_0 represents the background intensity of the fringe pattern, A is the modulation intensity of the fringe pattern, and $\varphi(x, y)$ denotes the phase of Newton’s rings interference fringes, which is given by $\varphi(x, y) = K\pi[(x - x_0)^2 + (y - y_0)^2] + \pi$, where $K = \frac{2}{\lambda R}$, and where λ is the wavelength of the incident light, and R is the radius of curvature of the lens under test. (x_0, y_0) represent the coordinates of the center of the Newton’s rings.

In this experiment, the Newton ring fringe parameters are set to $I_0 = 2$, $A = 2$, $\lambda = 600 \times 10^{-9}$, $R = 0.4$, and $(x_0, y_0) = (0, 0)$. We simulate Newton fringe patterns with a pixel dimension of 200×200 , each corrupted by white Gaussian noise. The proposed optimal filtering method is then applied to denoise the image.

The results of the optimal filtering in different transform domains, under various SNRs, are summarized in Table 5.3. The table presents the MSE, PSNR and SSIM values, along with the corresponding optimal parameters for each transform domain. As shown in the table, the optimal filtering in the 2D NSFRFT domain consistently outperforms those in the 2D FT, 2D SFRFT, GT, and CFRFT domains, achieving lower MSE, higher PSNR, and higher SSIM values. This demonstrates the effectiveness of the 2D NSFRFT-based optimal filtering in denoising the simulated Newton fringe pattern.

Table 5.3

Optimal filtering performance for simulated Newton fringe patterns in different transform domains under various SNRs

Transform	MSE / PSNR / SSIM (Optimal parameters)		SNR				
	−15	−10	−5	0	5	10	15
FT	−0.1047/1.0775/0.5034	−0.3649/3.7245/0.6443	−0.6780/6.8984/0.7592	−1.0209/10.3504/0.8460	−1.3776/13.9087/0.9053	−1.7390/17.5144/0.9433	−2.1082/21.1903/0.9665
2D SFRFT	−0.1407/1.4778/0.5170 (1.5729, 1.5848)	−0.4213/4.2745/0.6584 (1.5692, 1.6790)	−0.6978/7.1205/0.7645 (1.5725, 1.5830)	−1.0347/10.4952/0.8481 (1.5674, 1.5611)	−1.3933/14.0603/0.9059 (1.5653, 1.5660)	−1.7563/17.6698/0.9457 (1.5651, 1.5662)	−2.1243/21.3455/0.9682 (1.5620, 1.5833)
GT	−0.1229/1.2737/0.5189 (1.5699)	−0.3791/3.8713/0.6526 (1.5706)	−0.6856/6.9696/0.7623 (1.5699)	−1.0219/10.3488/0.8460 (1.5698)	−1.3731/13.8587/0.9039 (1.5694)	−1.7327/17.4532/0.9425 (−1.5708)	−2.1114/21.2195/0.9672 (−1.5703)
CFRFT	−0.1522/1.6037/0.5341 (1.5876, 1.5852)	−0.4224/4.4022/0.6806 (1.5912, 1.5909)	−0.7257/7.3949/0.7765 (1.5637, 1.5638)	−1.0281/10.4210/0.8485 (1.5630, 1.5630)	−1.3923/14.0512/0.9057 (1.5666, 1.5666)	−1.7523/17.6367/0.9445 (1.5630, 1.5630)	−2.1235/21.3377/0.9683 (1.5632, 1.5628)
2D NSFRFT	−0.1654/1.7150/0.5349 (0.9999, −0.0008, −0.0064, −0.0001, 1.5794)	−0.5355/5.4978/0.7318 (0.9999, 0.0004, −0.0024, 0, 1.5804)	−0.7374/7.5119/0.7806 (0.9999, −0.0005, −0.0066, 0.0001, 1.5754)	−1.0515/10.6716/0.8501 (0.9999, −0.0001, 0.0028, 0, 1.5637)	−1.4005/14.1423/0.9067 (0.9999, −0.0003, 0.0030, 0, 1.5637)	−1.7566/17.6766/0.9461 (0.9999, 0.0001, −0.0103, −0.0001, 1.5724)	−2.1263/21.3642/0.9684 (0.9999, −0.0001, −0.0114, −0.0001, 1.5725)

(3) Real-world image denoising

We choose six publicly available datasets to further validate the effectiveness of the proposed optimal filtering method, including SSID, O_HAZE, I_HAZE, OTS_BETA, ITS_V2 and Rain_100H. From each dataset, two images are randomly selected and resized to 256×256 pixels. An optimal filtering method is individually applied to the R, G, and B channels of each image.

The results in different transform domains are summarized in Table 5.4. The table reports MSE, PSNR and SSIM values for each dataset across five transform domains: 2D FT, 2D

SFRFT, GT, CFRFT, and 2D NSFRFT. Although the performance improvements are modest, the 2D NSFRFT-based optimal filtering consistently performs slightly better, achieving lower MSE, higher PSNR, and higher SSIM across all datasets. This suggests that the 2D NSFRFT-based optimal filtering offers a minor but consistent improvement over the other methods, demonstrating its potential for denoising real-world images.

Table 5.4

Denoising performance for real-world images from different datasets in various transform domains

Dataset	Index	MSE / PSNR / SSIM					
		Noisy Image and Original Image	FT	2D SFRFT	GT	CFRFT	2D NSFRFT
SSID	48	-1.4381/14.3806/0.5981	-2.4091/24.0907/0.7583	-2.4236/24.2357/0.7641	-2.3549/23.5491/0.7225	-2.4204/24.2037/0.7600	-2.4236/24.2364/0.7642
	165	-1.8268/18.2681/0.2656	-2.8460/28.4603/0.8421	-2.8520/28.5202/0.8457	-2.7782/27.7822/0.8095	-2.8537/28.5375/0.8453	-2.8575/28.5746/0.8461
O_HAZE	02	-1.4381/14.3806/0.5981	-1.4169/14.1694/0.4858	-2.0644/20.6435/0.8512	-2.0541/20.5410/0.8333	-2.0626/20.6263/0.8480	-2.0645/20.6449/0.8513
	45	-1.2334/12.3337/0.2616	-1.2237/12.2367/0.2092	-2.5494/25.4939/0.8811	-2.5160/25.1601/0.8507	-2.5493/25.4935/0.8811	-2.5506/25.5059/0.8814
I_HAZE	01	-1.3918/13.9185/0.6265	-1.3818/13.8181/0.5812	-2.1295/21.2950/0.8859	-2.0993/20.9927/0.8541	-2.1294/21.2936/0.8859	-2.1523/21.5228/0.8873
	03	-1.5540/15.5395/0.4369	-1.5396/15.3957/0.3383	-2.1883/21.8826/0.8792	-2.1605/21.6045/0.8402	-2.1882/21.8821/0.8793	-2.1894/21.8937/0.8798
OTS.BETA	25	-1.1757/11.7567/0.6017	-1.1614/11.6144/0.5127	-2.4626/24.6255/0.8825	-2.4271/24.2709/0.8284	-2.4737/24.7370/0.8754	-2.5682/25.6818/0.9223
	58	-1.3298/13.2984/0.6882	-1.2972/12.9716/0.5306	-2.6792/26.7922/0.8973	-2.6054/26.0542/0.8601	-2.6114/26.1139/0.8486	-2.7838/27.8383/0.9486
ITS.V2	02	-0.9895/9.8952/0.6692	-0.9822/9.8220/0.5808	-2.5187/25.1867/0.8708	-2.6329/26.3286/0.9169	-2.6327/26.3270/0.9166	-2.6348/26.3484/0.9183
	04	-1.7656/17.6560/0.8159	-1.7527/17.5271/0.7940	-2.1703/21.7035/0.8777	-2.3566/23.5657/0.9137	-2.3927/23.9267/0.9346	-2.4001/24.0008/0.9347
Rain_100H	08	-0.9843/9.8433/0.3517	-1.0543/10.5433/0.6086	-2.1245/21.2448/0.6915	-2.1438/21.4377/0.7185	-2.1559/21.5585/0.7266	-2.1623/21.6228/0.7300
	77	-1.0006/10.0059/0.4461	-1.0727/10.7270/0.5617	-1.8512/18.5119/0.7503	-1.8780/18.7800/0.7624	-1.8984/18.9840/0.7837	-1.8988/18.9880/0.7840

5.2.2. Passband and stopband filters. As demonstrated in Section III-D, the 2D NSFRFT possesses a unique ability to handle specific 2D chirp signals with nonseparable terms, an advantage that conventional transforms such as the 2D FT, 2D SFRFT, GT, and CFRFT lack. This capability is particularly significant because such 2D chirp signals with nonseparable terms are commonly encountered in real-world applications, including radar, communications, sonar, and optical imaging. Therefore, it becomes both necessary and meaningful to design dedicated filters for this class of signals. Moreover, the structure of the 2D NSFRFT makes it straightforward to construct passband and stopband filters, enabling effective noise suppression. The corresponding algorithmic pseudocode for filter design based on the 2D NSFRFT is provided in [Algorithm 5.2](#).

In the following, we designed two types of experiments to exploit this advantage:

- Removing noise from synthetic 2D chirp signals;
- Removing 2D chirp artifacts acting as structured interference in images.

These experiments aim to demonstrate the practical filtering superiority of the 2D NSFRFT when nonseparable terms are present.

(1) Removing noise from synthetic 2D chirp signals

We construct two synthetic 2D chirp signals with distinct quadratic phase structures, each containing nonseparable term, and add additive Gaussian noise to evaluate the denoising performance of the proposed method.

Algorithm 5.2 Bandpass and bandstop filter design using 2D NSFRFT for 2D chirp signals with nonseparable terms

Input: $f(x, y)$, Filter_Type (Bandpass or Bandstop), B (Bandwidth), Parameters $P = (a, b, c, d, \theta)$

Output: $f_{\text{filtered}}(x, y)$

Step 1: Compute the 2D NSFRFT of $f(x, y)$ to obtain $F_P(u, v)$

Step 2: Search for the impulse (peak) in the 2D NSFRFT domain

$\text{Impulse_Location} = \text{Find_Impulse}(F_P(u, v))$

Step 3: If the 2D Chirp signal is the signal to be preserved (i.e., it is not noise):

if is_useful(f) then

Step 4: Design a bandpass filter $H(u, v)$ around the impulse location

$H(u, v) = \text{Bandpass_Filter}(\text{Impulse_Location}, B)$

else

Step 5: Design a bandstop filter $H(u, v)$ to remove the impulse

$H(u, v) = \text{Bandstop_Filter}(\text{Impulse_Location}, B)$

end if

Step 6: Apply the designed filter to the transformed signal

$F_{\text{filtered}}(u, v) = F_P(u, v)H(u, v)$

Step 7: Perform the inverse 2D NSFRFT to obtain the filtered image

$f_{\text{filtered}}(x, y) = (\mathcal{F}_P)^{-1}[F_{\text{filtered}}(u, v)](x, y)$

The first 2D chirp signal is $f_1(x, y) = \exp(-j(0.866x^2 - 2xy + 0.866y^2))$, which contains strong nonseparable term. Gaussian white noise with SNR = -5 dB is added. The parameter set for the 2D NSFRFT is given by $P_1 = (\frac{1}{2}, \frac{1}{2}, \frac{1}{2}, \frac{1}{2}, \frac{\pi}{3})$. The filtering results under different transform domains are shown in the first row of Figure 5.4. The second 2D chirp signal is $f_2(x, y) = \exp(j(0.2897x^2 + 0.0061xy + 0.2877y^2))$, which exhibits weaker nonseparable term. Gaussian white noise with SNR = -10 dB is added. The parameter set for the 2D NSFRFT is given by $P_2 = (-0.0046, 0.0016, -0.0241, 0.9997, \frac{\pi}{6})$. The corresponding denoising results are shown in the second row of Figure 5.4.

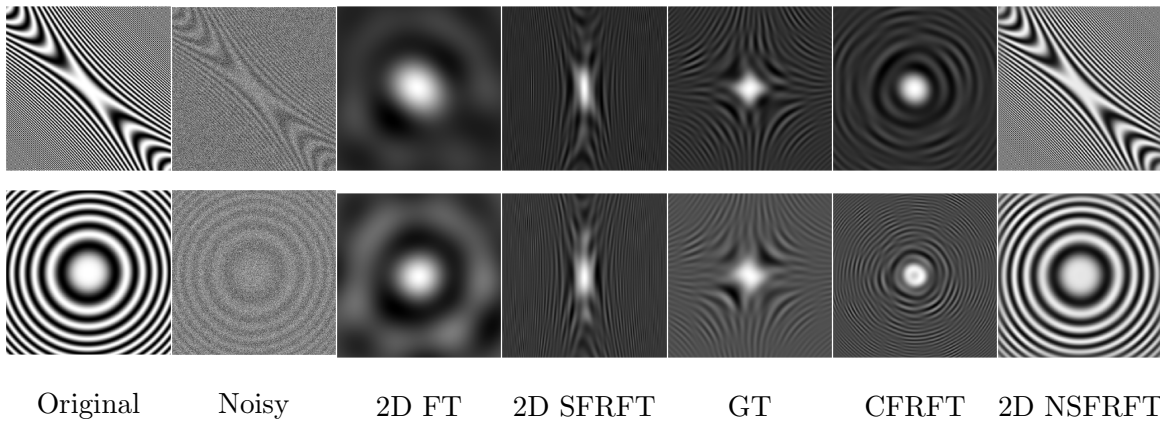


Figure 5.4. Denoising synthetic 2D chirp signals with nonseparable terms in different transform domains.

These results demonstrate that the 2D NSFRFT-based passband filter achieves superior restoration quality compared to traditional transform-domain methods when nonseparable terms are present.

(2) Removing 2D chirp artifacts acting as structured interference in images

In addition to being useful signal models, 2D chirp signals containing nonseparable terms can also act as structured artifacts that degrade image quality in various applications, such as interferometric imaging, raster-scanned images, and computed tomography. It is therefore important to effectively suppress such artifacts when they appear in these scenarios.

As shown in Figure 5.5, two clean images are respectively corrupted by different 2D chirp signals, resulting in structured artifacts. The interference signals are $f_3 = \exp(j(0.2816x^2 + 0.1552xy + 0.3064y^2 + 5.4319x - 6.7898y))$ and $f_4 = \exp(j(0.2639x^2 + 0.3552xy + 0.2660y^2 + 6.7789x + 0.0678y))$, respectively. And the corresponding 2D NSFRFT parameter sets are set to $P_3 = (-0.0692, 0.0938, -0.8823, 0.4560, \frac{\pi}{6})$ and $P_4 = (0.1019, -0.2525, 0.8944, -0.3548, \frac{\pi}{7})$.

By applying a stopband filter in the 2D NSFRFT domain, we remove the interference components. The restored images after filtering are also shown in Figure 5.5, demonstrating that the proposed method effectively eliminates the chirp-based artifacts while preserving the underlying image structures.

As illustrated in Figure 5.5, all five transform-domain filtering methods are applied to remove the structured 2D chirp artifacts. Compared with the 2D FT, 2D SFRFT, GT, and CFRFT, the proposed 2D NSFRFT-based band-stop filter achieves notably better artifact suppression. In particular, while other methods leave behind significant residual interference or cause visible distortion to the underlying image structures, the 2D NSFRFT-based approach effectively removes most chirp artifacts. This further validates the advantage of the 2D NSFRFT in handling nonseparable interference components that are difficult to isolate in conventional transform domains.

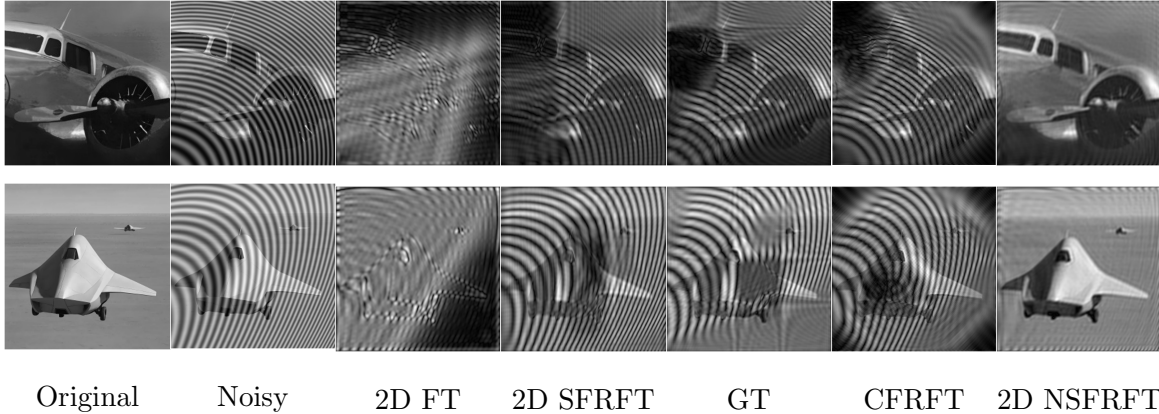


Figure 5.5. Removal of 2D chirp artifacts acting as structured interference using different transform-domain filters.

6. Conclusion. This paper introduces the 2D NSFRFT, which incorporates four degrees of freedom. This definition not only encompasses the 2D SFRFT, GT, and CFRFT as special

cases but also offers more general time-frequency plane rotation characteristics, thereby significantly enhancing the theoretical completeness and applicability of 2D non-stationary signal processing. Additionally, the properties of the 2D NSFRFT are derived, and a direct discrete algorithm, along with two fast algorithms, are discussed. These fast algorithms exhibit computational complexity comparable to that of the 2D SFRFT. In terms of applications, a DRPED method based on the 2D NSFRFT is proposed, which significantly enhances security by exploiting the additional degrees of freedom and greater flexibility of the 2D NSFRFT. The correctness and effectiveness of this method are validated through simulations. Moreover, in filter design, we consider two types of filters: the first is an optimal filter, and the second is a bandpass and bandstop filter designed specifically for the 2D chirp signals with nonseparable terms, numerical simulations and comparative experiments consistently demonstrate that the 2D NSFRFT achieves superior performance compared to the 2D FT, 2D SFRFT, GT, and CFRFT. This work provides new theoretical support for the 2D FRFT, extending the understanding of its time-frequency rotation characteristics and establishing it as a unified framework that encompasses the 2D SFRFT, GT, and CFRFT as special cases. The 2D NSFRFT broadens the applicability of signal processing in engineering practice, particularly in areas such as image encryption, decryption, filtering, and denoising. The numerical results presented in this study confirm that the 2D NSFRFT achieves significant improvements over existing 2D FRFTs, highlighting its potential to play a crucial role in future 2D signal processing applications.

Appendix A. Proof of 2D NSFRFT for processing 2D chirp signals with nonseparable terms.

Proof. Considering the 2D chirp signal with a nonseparable term given by

$$(A.1) \quad f(x, y) = e^{-\frac{j(p_1 x^2 + p_2 xy + p_3 y^2)}{2\mathbf{T}}},$$

by substituting (A.1) into the 2D NSFRFT defined in (3.1), and applying the kernel expression from (3.2), after some simplification, we have

$$(A.2) \quad F_{(a,b,c,d,\theta)}(u, v) = \frac{1}{2\pi\sqrt{-\mathbf{T}}} e^{\frac{j(k_1 u^2 + k_2 uv + k_3 v^2)}{2\mathbf{T}}} \int_{\mathbb{R}^2} e^{\frac{j(m_1 ux + m_2 vx + m_3 uy + m_4 vy)}{\mathbf{T}}} dx dy.$$

Next, we consider the remaining part of the integral, by utilizing the properties of the 2D FT and the Dirac delta function yields

$$(A.3) \quad \int_{\mathbb{R}^2} e^{\frac{j(m_1 ux + m_2 vx + m_3 uy + m_4 vy)}{\mathbf{T}}} dx dy = (2\pi)^2 |\mathbf{T}|^2 \delta(m_1 u + m_2 v) \delta(m_3 u + m_4 v).$$

Combining the coefficient terms, we obtain

$$(A.4) \quad \frac{(2\pi)^2 |\mathbf{T}|^2}{2\pi\sqrt{-\mathbf{T}}} = \frac{2\pi\mathbf{T}^2}{\sqrt{-\mathbf{T}}}.$$

Substituting (A.3) and (A.4) into (A.2), the final result of the 2D NSFRFT of $f(x, y)$ is

$$F_{(a,b,c,d,\theta)}(u, v) = \frac{2\pi\mathbf{T}^2}{\sqrt{-\mathbf{T}}} e^{\frac{j(k_1 u^2 + k_2 uv + k_3 v^2)}{2\mathbf{T}}} \delta(m_1 u + m_2 v) \delta(m_3 u + m_4 v).$$

This completes the proof. ■

REFERENCES

- [1] L. B. ALMEIDA, *The fractional Fourier transform and time-frequency representations*, IEEE Trans. Signal Process., 42 (1994), pp. 3084–3091.
- [2] D. H. BAILEY AND P. N. SWARZTRAUBER, *The fractional Fourier transform and applications*, SIAM Rev., 33 (1991), pp. 389–404, <https://doi.org/10.1137/1033097>.
- [3] D. H. BAILEY AND P. N. SWARZTRAUBER, *A fast method for the numerical evaluation of continuous Fourier and Laplace transforms*, SIAM J. Sci. Comput., 15 (1994), pp. 1105–1110, <https://doi.org/10.1137/0915067>.
- [4] R. G. CAMPOS, J. RICO-MELGOZA, AND E. CHÁVEZ, *A new formulation of the fast fractional Fourier transform*, SIAM J. Sci. Comput., 34 (2012), pp. A1110–A1125, <https://doi.org/10.1137/100812677>.
- [5] J. Y. CHEN AND B. Z. LI, *Wigner distribution associated with linear canonical transform of generalized 2-D analytic signals*, Digit. Signal Process., 149 (2024), p. 104481.
- [6] E. CORDERO, M. DE GOSSON, M. DÖRFLER, AND F. NICOLA, *On the symplectic covariance and interferences of time-frequency distributions*, SIAM J. Math. Anal., 50 (2018), pp. 2178–2193, <https://doi.org/10.1137/16M1104615>.
- [7] L. DEBNATH AND L. DEBNATH, *The Wigner-Ville distribution and time-frequency signal analysis*, Wavelet Transf. Appl., (2002), pp. 307–360.
- [8] J. J. DING, S. C. PEI, AND C. L. LIU, *Improved implementation algorithms of the two-dimensional nonseparable linear canonical transform*, J. Opt. Soc. Amer. A, 29 (2012), pp. 1615–1624.
- [9] M. F. ERDEN, M. A. KUTAY, AND H. M. OZAKTAS, *Repeated filtering in consecutive fractional Fourier domains and its application to signal restoration*, IEEE Trans. Signal Process., 47 (1999), pp. 1458–1462.
- [10] Z. FU, Y. LIN, D. YANG, AND S. YANG, *Fractional Fourier transforms meet Riesz potentials and image processing*, SIAM J. Imaging Sci., 17 (2024), pp. 476–500, <https://doi.org/10.1137/23M1555442>.
- [11] E. GARZA-FLORES AND J. ÁLVAREZ-BORRERO, *Pattern recognition using binary masks based on the fractional Fourier transform*, J. Mod. Opt., 65 (2018), pp. 1634–1657.
- [12] F. GOUDAIL, F. BOLLARO, B. JAVIDI, AND P. RÉFRÉGIER, *Influence of a perturbation in a double phase-encoding system*, J. Opt. Soc. Amer. A, 15 (1998), pp. 2629–2638.
- [13] J. HAHN, H. KIM, AND B. LEE, *Optical implementation of iterative fractional Fourier transform algorithm*, Opt. Express, 14 (2006), pp. 11103–11112.
- [14] P. HAMMACHUKIATTIKUL, A. MOHANAPRIYA, A. GANESH, G. RAJCHAKIT, V. GOVINDAN, N. GUNASEKARAN, AND C. P. LIM, *A study on fractional differential equations using the fractional Fourier transform*, Adv. Differ. Equ., 2020 (2020), pp. 1–22.
- [15] B. HENNELLY AND J. T. SHERIDAN, *Fractional Fourier transform-based image encryption: phase retrieval algorithm*, Opt. Commun., 226 (2003), pp. 61–80.
- [16] A. KOÇ, H. M. OZAKTAS, AND L. HESSELINK, *Fast and accurate computation of two-dimensional non-separable quadratic-phase integrals*, J. Opt. Soc. Amer. A, 27 (2010), pp. 1288–1302.
- [17] E. KOÇ, T. ALIKASIFOGLU, A. C. ARAS, AND A. KOÇ, *Trainable fractional Fourier transform*, IEEE Signal Process. Lett., (2024).
- [18] A. KUTAY, H. M. OZAKTAS, O. ANKAN, AND L. ONURAL, *Optimal filtering in fractional Fourier domains*, IEEE Trans. Signal Process., 45 (1997), pp. 1129–1143.
- [19] J. LANG, R. TAO, AND Y. WANG, *Image encryption based on the multiple-parameter discrete fractional Fourier transform and chaos function*, Opt. Commun., 283 (2010), pp. 2092–2096.
- [20] J. B. LIMA AND L. NOVAES, *Image encryption based on the fractional Fourier transform over finite fields*, Signal Process., 94 (2014), pp. 521–530.
- [21] M. F. LU, G. Q. NI, T. Z. BAI, R. TAO, AND F. ZHANG, *Method for suppressing the quantization error of newton's rings fringe pattern*, Opt. Eng., 52 (2013), pp. 103105–103105.
- [22] M. F. LU, G. Q. NI, T. WANG, F. ZHANG, R. TAO, AND J. YUAN, *Method for reducing newton's rings pattern in the scanned image reproduced with film scanners*, in 2013 International Conference on Optical Instruments and Technology: Optoelectronic Imaging and Processing Technology, vol. 9045, SPIE, 2013, pp. 32–41.
- [23] M. F. LU, J. M. WU, F. ZHANG, AND R. TAO, *Chirp images in 2-d fractional Fourier transform domain*, in 2016 IEEE International Conference on Signal Processing, Communications and Computing

- (ICSPCC), IEEE, 2016, pp. 1–4.
- [24] T. C. MAHOR, R. MISHRA, AND R. JAIN, *Analytical solutions of linear fractional partial differential equations using fractional Fourier transform*, J. Comput. Appl. Math., 385 (2021), p. 113202.
 - [25] A. MCBRIDE AND F. KERR, *On namias's fractional Fourier transforms*, IMA J. Appl. Math., 39 (1987), pp. 159–175.
 - [26] J. E. MEBIUS, *Derivation of the euler-rodrigues formula for three-dimensional rotations from the general formula for four-dimensional rotations*, arXiv:math/0701759, (2007).
 - [27] O. MELNYK AND P. RÖMER, *Background removal for Ptychography via Wigner distribution deconvolution*, SIAM J. Imaging Sci., 17 (2024), pp. 1978–2014, <https://doi.org/10.1137/24M1642433>.
 - [28] D. MENDLOVIC AND H. M. OZAKTAS, *Fractional Fourier transforms and their optical implementation: I*, J. Opt. Soc. Amer. A, 10 (1993), pp. 1875–1881.
 - [29] D. MENDLOVIC, Z. ZALEVSKY, AND H. M. OZAKTAS, *Applications of the fractional Fourier transform to opt. pattern recognit.*, Opt. Pattern Recognit., (1998), pp. 89–125.
 - [30] A. NAJMI, *The Wigner distribution: A time-frequency analysis tool*, Johns Hopkins APL Tech. Dig., 15 (1994), pp. 298–298.
 - [31] V. NAMIAS, *The fractional order Fourier transform and its application to quantum mechanics*, IMA J. Appl. Math., 25 (1980), pp. 241–265.
 - [32] H. M. OZAKTAS, O. ARIKAN, M. A. KUTAY, AND G. BOZDAGT, *Digital computation of the fractional Fourier transform*, IEEE Trans. Signal Process., 44 (1996), pp. 2141–2150.
 - [33] H. M. OZAKTAS, B. BARSHAN, D. MENDLOVIC, AND L. ONURAL, *Convolution, filtering, and multiplexing in fractional Fourier domains and their relation to chirp and wavelet transforms*, J. Opt. Soc. Amer. A, 11 (1994), pp. 547–559.
 - [34] H. M. OZAKTAS, N. ERKAYA, AND M. A. KUTAY, *Effect of fractional Fourier transformation on time-frequency distributions belonging to the cohen class*, IEEE Signal Process. Lett., 3 (1996), pp. 40–41.
 - [35] H. M. OZAKTAS AND D. MENDLOVIC, *Fractional Fourier transforms and their optical implementation: II*, J. Opt. Soc. Am. A, 10 (1993), pp. 2522–2531.
 - [36] H. M. OZAKTAS AND D. MENDLOVIC, *Fractional Fourier optics*, J. Opt. Soc. Amer. A, 12 (1995), pp. 743–751.
 - [37] H. M. OZAKTAS, Z. ZALEVSKY, AND M. A. KUTAY, *The Fractional Fourier Transform with Applications in Optics and Signal Process.*, J. Wiley & Sons, 2001.
 - [38] S. C. PEI, *Two-dimensional affine generalized fractional Fourier transform*, IEEE Trans. Signal Process., 49 (2001), pp. 878–897.
 - [39] S. C. PEI AND J. J. DING, *Relations between fractional operations and time-frequency distributions, and their applications*, IEEE Trans. Signal Process., 49 (2001), pp. 1638–1655.
 - [40] S. C. PEI AND S. G. HUANG, *Two-dimensional nonseparable discrete linear canonical transform based on CM-CC-CM-CC decomposition*, J. Opt. Soc. Amer. A, 33 (2016), pp. 214–227.
 - [41] S. C. PEI, S. G. HUANG, AND J. J. DING, *Discrete gyrator transforms: computational algorithms and applications*, IEEE Trans. Signal Process., 63 (2015), pp. 4207–4222.
 - [42] L. QI, R. TAO, S. Y. ZHOU, AND Y. WANG, *Detection and parameter estimation of multicomponent LFM signal based on the fractional Fourier transform*, Sci. China Ser. F, 47 (2004), pp. 184–198.
 - [43] J. RAMANATHAN AND P. TOPIWALA, *Time-frequency localization via the Weyl correspondence*, SIAM J. Math. Anal., 24 (1993), pp. 1378–1393, <https://doi.org/10.1137/0524080>.
 - [44] J. A. RODRIGO, T. ALIEVA, AND M. L. CALVO, *Gyrator transform: properties and applications*, Opt. Express, 15 (2007), pp. 2190–2203.
 - [45] A. SAHIN, M. A. KUTAY, AND H. M. OZAKTAS, *Nonseparable two-dimensional fractional Fourier transform*, Appl. Opt., 37 (1998), pp. 5444–5453.
 - [46] A. SAHIN, H. M. OZAKTAS, AND D. MENDLOVIC, *Optical implementations of two-dimensional fractional Fourier transforms and linear canonical transforms with arbitrary parameters*, Appl. Opt., 37 (1998), pp. 2130–2141.
 - [47] A. SAHIN, H. M. OZAKTAS, AND D. MENDLOVIC, *Optical implementations of two-dimensional fractional Fourier transforms and linear canonical transforms with arbitrary parameters*, Appl. Opt., 37 (1998), pp. 2130–2141.
 - [48] F. ŞAHINUÇ AND A. KOÇ, *Fractional Fourier transform meets transformer encoder*, IEEE Signal Process. Lett., 29 (2022), pp. 2258–2262.

- [49] J. SHI, J. B. ZHENG, X. P. LIU, W. XIANG, AND Q. Y. ZHANG, *Novel short-time fractional Fourier transform: Theory, implementation, and applications*, IEEE Trans. Signal Process., 68 (2020), pp. 3280–3295.
- [50] N. SINGH AND A. SINHA, *Optical image encryption using fractional Fourier transform and chaos*, Opt. Laser Eng., 46 (2008), pp. 117–123.
- [51] X. H. SU, R. TAO, AND Y. Z. LI, *Phase retrieval from multiple FRFT measurements based on nonconvex low-rank minimization*, Signal Process., 198 (2022), p. 108601.
- [52] R. TAO, B. Z. LI, AND Y. WANG, *Spectral analysis and reconstruction for periodic nonuniformly sampled signals in fractional Fourier domain*, IEEE Trans. Signal Process., 55 (2007), pp. 3541–3547.
- [53] R. TAO, X. Y. MENG, AND Y. WANG, *Image encryption with multiorders of fractional Fourier transforms*, IEEE Trans. Inf. Forensics Secur., 5 (2010), pp. 734–738.
- [54] A. TORRE, *The fractional Fourier transform and some of its applications to optics*, in Progress in Optics, vol. 43, Elsevier, 2002, pp. 531–596.
- [55] G. UNNIKRISHNAN, J. JOSEPH, AND K. SINGH, *Optical encryption by double-random phase encoding in the fractional Fourier domain*, Opt. Lett., 25 (2000), pp. 887–889.
- [56] D. Y. WEI AND Y. SHEN, *Fast numerical computation of two-dimensional non-separable linear canonical transform based on matrix decomposition*, IEEE Trans. Signal Process., 69 (2021), pp. 5259–5272.
- [57] D. Y. WEI AND J. YANG, *Two-dimensional sparse fractional Fourier transform and its applications*, Signal Process., 201 (2022), p. 108682.
- [58] J. M. WU, M. F. LU, R. TAO, F. ZHANG, AND Y. LI, *Improved frft-based method for estimating the physical parameters from newton's rings*, Opt. Lasers Eng., 91 (2017), pp. 178–186.
- [59] H. C. XIN AND B. Z. LI, *On a new Wigner-Ville distribution associated with linear canonical transform*, EURASIP J. Adv. Signal Process., 2021 (2021), p. 56.
- [60] Y. X. YANG AND R. TAO, *Single-shot fractional Fourier phase retrieval*, in ICASSP 2023-2023 IEEE International Conference on Acoustics, Speech and Signal Process. (ICASSP), IEEE, 2023, pp. 1–5.
- [61] Y. X. YANG, R. TAO, K. X. WEI, AND J. SHI, *Single-shot phase retrieval from a fractional Fourier transform perspective*, IEEE Trans. Signal Process., (2024).
- [62] L. YING AND S. FOMEL, *Fast computation of partial Fourier transforms*, Multiscale Model. Simul., 8 (2009), pp. 110–124, <https://doi.org/10.1137/080715457>.
- [63] Z. ZALEVSKY AND D. MENDLOVIC, *Fractional Wiener filter*, Appl. Opt., 35 (1996), pp. 3930–3936.
- [64] A. ZAYED, *Two-dimensional fractional Fourier transform and some of its properties*, Integr. Transf. Spec. Funct., 29 (2018), pp. 553–570.
- [65] A. ZAYED, *A new perspective on the two-dimensional fractional Fourier transform and its relationship with the Wigner distribution*, J. Fourier Anal. Appl., 25 (2019), pp. 460–487.
- [66] A. I. ZAYED, *Solution of the energy concentration problem in reproducing-kernel Hilbert space*, SIAM J. Appl. Math., 75 (2015), pp. 21–37, <https://doi.org/10.1137/140979460>.
- [67] A. I. ZAYED, *On the extension and sampling theorem for the coupled fractional Fourier transform*, in 2023 International Conference on Sampling Theory and Applications (SampTA), IEEE, 2023, pp. 1–4.
- [68] C. W. ZHANG, S. P. WANG, L. B. JIAO, J. SHI, AND J. YUE, *A novel mulora modulation based on fractional Fourier transform*, IEEE Commun. Lett., 25 (2021), pp. 2993–2997.
- [69] Z. C. ZHANG, D. LI, Y. F. HE, Y. J. CHEN, J. W. ZHANG, AND C. X. ZHOU, *K-Wigner distribution: definition, uncertainty principles and time-frequency analysis*, IEEE Trans. Inf. Theory, 69 (2022), pp. 2722–2736.
- [70] Z. C. ZHANG AND M. K. LUO, *New integral transforms for generalizing the Wigner distribution and ambiguity function*, IEEE Signal Process. Lett., 22 (2014), pp. 460–464.